ACS APPLIED MATERIALS & INTERFACES

www.acsami.org

Research Article

Donor–Acceptor Compensated ZnO Semiconductor for Photoelectrochemical Biosensors

Delun Chen, Xue Zou, Fan Dong, Chao Zhen,* Dan Xiao, Xiaohong Wang, Qiang Wu, Yang Cao, and Jinchun Tu*

Cite This: *ACS Appl. Mater. Interfaces* 2021, 13, 33006–33014

Read Online

ACCESS | Metrics & More | Article Recommendations | Supporting Information

ABSTRACT: Hindering the recombination of a photogenerated carrier is a crucial method to enhance the photoelectrochemical performance of ZnO due to its high exciton binding energy. Herein, the intramolecular donor–acceptor compensated semiconductor ZnO (I-D/A ZnO), introducing C dopants and oxygen vacancies, was prepared with the assistance of ascorbic acid (AA). According to the DFT calculations, the asymmetry DOS could lead to the longer carrier lifetime and the smaller electron transfer resistance. Then, the photoelectrochemical biosensor toward glucose was regarded as a model to discuss the application of ZnO in biosensors. As a result, the biosensor based on I-D/A ZnO showed good performance with high sensitivity, low limit of detection, and fine anti-interference, meaning that I-D/A ZnO is a promising semiconductor for photoelectrochemical biosensors.

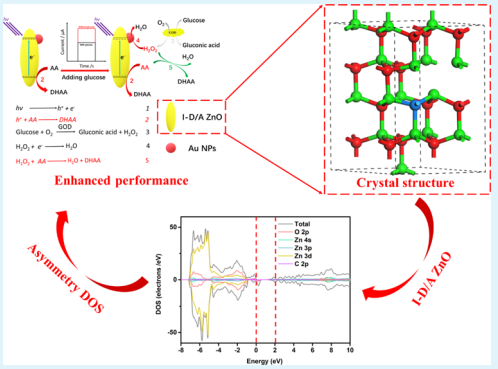

KEYWORDS: *zinc oxide, donor–acceptor compensated semiconductors, photoelectrochemical biosensors, oxygen vacancies, carbon doping*

1. INTRODUCTION

Photoelectrochemical technologies have been widely used in various fields including energy conversion,[1−4] detection,[5,6] and photoelectrochemical biosensors.[7−12] For photoelectrochemical biosensors, a consensus has been reached that the semiconductor plays the crucial roles in achieving high performances.[13−16] ZnO as a well-known semiconductor for photoelectrochemical technology could provide many advantages such as low toxicity, environmental sustainability, piezoelectric properties, and high electron mobility.[17−20] However, the large band gap of ZnO limits the light response range,[21] and large exciton binding energy results in the short lifetime of photogenerated carriers.[22] According to the literatures, C-doping could introduce the acceptor levels above the valence band maximum (VBM) in ZnO,[17,23,24] and oxygen vacancy could introduce the donor levels below the conduction band minimum (CBM).[25−28] As a result, both are the feasible methods to reduce the band gap and prolong the carrier lifetimes of ZnO, accordingly improving the photoelectrochemical performances. However, either C-doping or introducing oxygen vacancies in ZnO could not stabilize the photogenerated electrons and photogenerated holes simultaneously.

Building donor–acceptor (D/A)-conjugated organic semiconductors is an effective method toward adjusting the electronic structures of organic semiconductors. Due to the advantages in dissociating excitons,[29] spatially separating charges,[29] tuning the charge-transfer-based emission,[30] rapid charge transfer,[31] and generating long-lived charge-transfer states,[32] D/A-conjugated organic semiconductors have been extensively investigated and applied in solar energy conversion systems.[33−39] According to the research results of D/A-conjugated organic semiconductors and ZnO, it was proposed that the intramolecular D/A compensated semiconductor ZnO (I-D/A ZnO) with high performance could be prepared via C-doping and creating oxygen vacancies simultaneously because of the effectively dissociating excitons.

Herein, I-D/A ZnO containing C dopants and oxygen vacancies was prepared with the assistance of ascorbic acid (AA) in this work. The structures and photoelectrochemical performance of the resultant I-D/A ZnO have been systematically characterized. Then, the density functional theory (DFT) calculation was carried out to discuss the relationship between photoelectrochemical performances and the electronic structures of I-D/A ZnO. It found that I-D/A ZnO with the asymmetry DOS results in the longer carrier lifetime and the smaller electron transfer resistance, which lead to the better photoelectric performance. Finally, the glucose enzyme biosensor was constructed as a model to determine the

Received: April 23, 2021
Accepted: June 24, 2021
Published: July 7, 2021

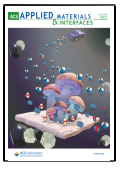

https://doi.org/10.1021/acsami.1c07499
ACS Appl. Mater. Interfaces 2021, 13, 33006−33014

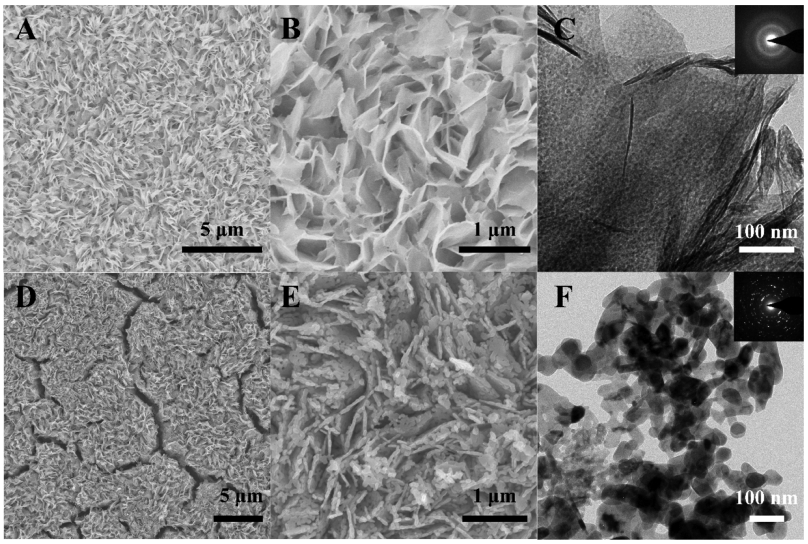

Figure 1. SEM images of AA−ZnHC (A,B) and I-D/A ZnO (D,E) and TEM images of AA−ZnHC (C) and I-D/A ZnO (F).

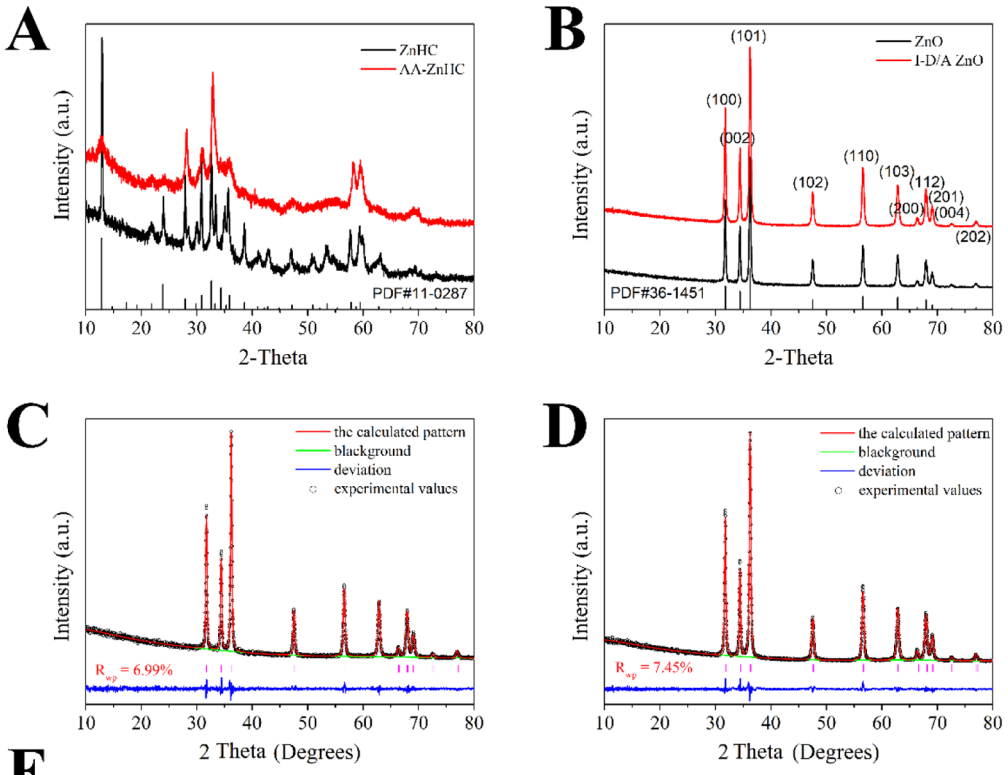

E XRD refinement results of ZnO and I-D/A ZnO

	a (Å)	b (Å)	c (Å)	grain size (nm)
ZnO	3.25139	3.251391	5.209942	62.1
I-D/A ZnO	3.2472	3.2472	5.203204	45.2

Figure 2. XRD spectra of (A) ZnHC and AA−ZnHC and (B) ZnO and I-D/A ZnO; XRD pattern refinements of (C) ZnO and (D) I-D/A ZnO; and (E) XRD refinement results of ZnO and I-D/A ZnO.

application potential of I-D/A ZnO in the photoelectrochemical biosensors.

2. EXPERIMENTAL SECTION

2.1. Preparation of I-D/A ZnO. All chemicals were analytical-grade reagents without further purification. In a typical experiment, a solution containing 40 mM $Zn(NO_3)_2{\cdot}6H_2O$, 0.2 M urea, 50 mM cetyltrimethlammonium bromide (CTAB), and 5 mM AA was prepared. Then, the aforementioned solution and the cleaned FTO were transferred into a Teflon-lined autoclave at 100 °C for 6 h. Then, the sample was marked as AA−ZnHC. Subsequently, AA−ZnHC was calcinated at 350 °C for 6 h to obtain I-D/A ZnO. For comparison,

https://doi.org/10.1021/acsami.1c07499
ACS Appl. Mater. Interfaces 2021, 13, 33006−33014

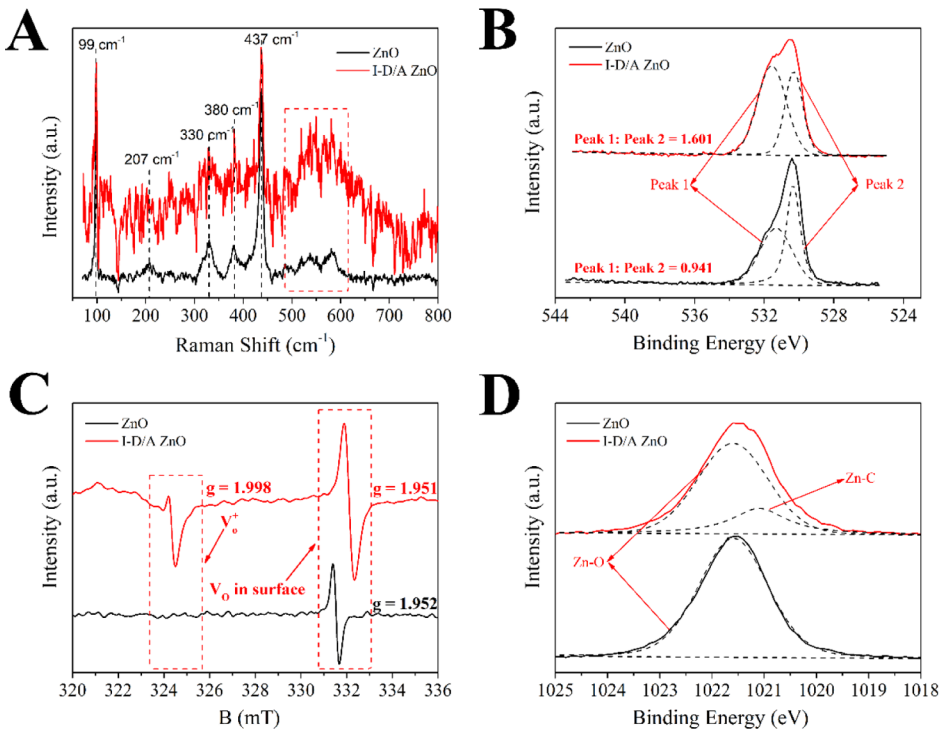

Figure 3. (A) Raman spectra, (B) O 1s high-resolution XPS spectra, (C) EPR spectra, and (D) Zn 2p resolution XPS spectra of ZnO and I-D/A ZnO.

ZnO was prepared without AA, and the detail is given in the Supporting Information.

2.2. Fabrication of the Photoelectrochemical Biosensor Electrode. The photoelectrochemical biosensor was fabricated as follows: 50 μL of Au nanoparticles (Au NPs, the synthesis process is given in the Supporting Information) was deposited onto the surface of I-D/A ZnO and dried at 50 °C. Then, 20 μL of glucose oxidase (GOD, 10 mg/mL) was deposited onto its surface and stored at 4 °C. The detection performance toward glucose was investigated using the electrolyte containing 10 mM AA, and the details are given in the Supporting Information.

3. RESULTS AND DISCUSSION

As shown in Figure 1, AA−ZnHC (Figure 1A,B) is composed of nanoflakes and the morphology could be maintained after annealing (Figure 1D,E). Compared with the samples of ZnHC and ZnO (Figure S1), both AA−ZnHC and I-D/A ZnO show nanoflakes being thinner in a high density of growth. Furthermore, the nanoflakes of I-D/A ZnO are made of nanoparticles (Figure 1F), but the nanoflakes of ZnO are complete units with nanopores (Figure S1F). In addition, HRTEM was used to analyze the crystalline interplanar spacing of the samples. According to Figure S2, the crystalline interplanar spacing of ZnHC and AA−ZnHC was related to $Zn_4CO_3(OH)_6{\cdot}H_2O$ (PDF#11-0287), while the crystalline interplanar spacing of ZnO and I-D/A ZnO belongs to (101) in ZnO (PDF#36-1451). Meanwhile, the lattice fringes of I-D/A ZnO was unclear compared with that of ZnO, suggesting the low crystallinity of I-D/A ZnO, which is consistent with the results of SAED (inset in Figures 1 and S1).

The XRD patterns of ZnHC and AA−ZnHC belong to $Zn_4CO_3(OH)_6{\cdot}H_2O$ (PDF#11-0287) without any impurity peaks (Figure 2A). The broadened peaks of AA-ZnHC indicate its low crystallinity (Figure 2A), in accordance with the TEM results (Figures 1 and S1). After annealing, the peaks of ZnO and I-D/A ZnO (Figure 2B) were assigned to wurtzite ZnO (*P*63*mc*, PDF#36-1451). To analyze the difference of the fine structure between I-D/A ZnO and ZnO, the XRD refinement has been employed,[40] and the results are shown in Figure 2C−E. The XRD spectra of ZnO and I-D/A ZnO could be fitted well with the acceptable R_w of 6.99% (Figure 2C) and 7.45% (Figure 2D), respectively. However, the crystal lattice parameters extracted from the refinement results of I-D/A ZnO are shrunken as compared with those of ZnO, which may be resulted from the defect production in the crystal lattice. Moreover, the grain size of I-D/A ZnO becomes smaller due to the high nucleation rate when AA was added.

Raman, XPS, and EPR were implemented (Figure 3) to investigate the defects in I-D/A ZnO and ZnO. The peaks in Raman spectra at 99 and 437 cm^{-1} are assigned to wurtzite ZnO (Figure 3A), while the broadened peaks from 500 to 600 cm^{-1} are attributed to the oxygen defects.[41,42] In addition, the peak area of I-D/A ZnO from 500 to 600 cm^{-1} is larger than that of ZnO, which suggests that more oxygen defects appeared in I-D/A ZnO compared with ZnO. Furthermore, the oxygen defects were characterized by XPS and EPR. In the O 1s XPS spectra (Figure 3B), the peak 1 at ∼531.6 eV belongs to the loosely bound oxygen in the defects, and the peak 2 at ∼530.3 eV belongs to the lattice oxygen. Then, the higher area ratio of the peak 1 for I-D/A ZnO indicates the larger number of loosely bound oxygen in I-D/A ZnO. Meanwhile, more oxygen vacancies in I-D/A ZnO could be confirmed from the EPR results. The stronger peak near g = 1.95 for I-D/A ZnO in comparison with that for ZnO at the EPR spectra suggests more oxygen vacancies in the surface (Figure 3C). Meanwhile, an additional peak at g = 1.998 in EPR of I-D/A ZnO (Figure 3C) explains the existence of V_O^+ in the sample. Based on the abovementioned systematic analysis, I-D/A ZnO contains more oxygen vacancies compared with ZnO. To clarify the chemical states of C in samples, Zn 2p high-resolution XPS spectra were recorded

https://doi.org/10.1021/acsami.1c07499
ACS Appl. Mater. Interfaces 2021, 13, 33006−33014

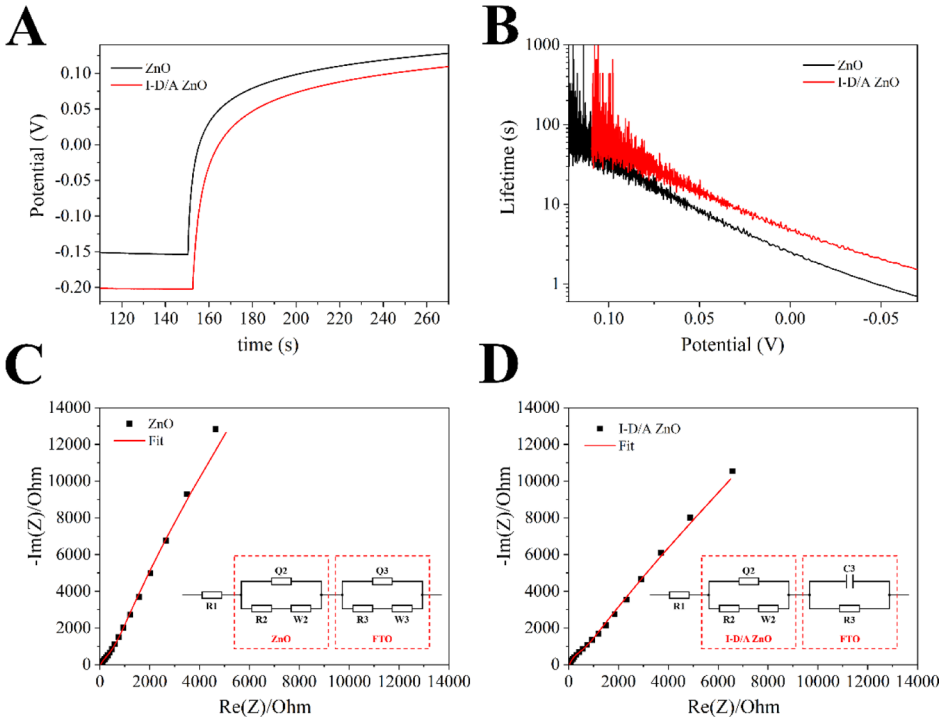

Figure 4. (A) Open-circuit photovoltage decay curves and (B) lifetime of photogenerated carriers of ZnO and I-D/A ZnO; EIS spectra and their equivalent circuits of (C) ZnO and (D) I-D/A ZnO.

(Figure 3D). Two peaks could be recognized from the Zn 2p XPS peak (Figure 3D) in I-D/A ZnO, which correspond to Zn−O and Zn−C bonds and indicating that carbon was doped in I-D/A ZnO. Meanwhile, only one peak belonging to the Zn−O bond could be found in the XPS of Zn 2p in ZnO (Figure 3D), negating the C-dopants in ZnO. In addition, photoluminescence (PL) spectroscopy is an important method to characterize the defects in ZnO. According to the result (Figure S3D), the PL peaks at ∼513.2 and ∼523.2 nm are attributed to the existence of different oxygen vacancies. However, a new peak at 492.4 nm could be only found in I-D/A ZnO, which is due to the C-dopants in I-D/A ZnO.

Based on the abovementioned analysis, addition of AA during the preparation process could lead to low crystallinity, small grain size, and the coexistence of C-doping and oxygen vacancies in I-D/A ZnO. Actually, AA plays the essential roles in adjusting morphology and composition of ZnO during the synthesis. When AA was added, the complex $\{$CTAB−AA−Zn^{2+}−AA$\}_n$ formed, which could hinder the desorption of CTAB from ZnHC.[43] Therefore, the crystals grow slowly and the fusion among crystals is obstructed. Consequently, I-D/A ZnO shows low crystallinity and small grain size. On the other hand, AA is an effective reducing agent and usually used as a carbon dopant source, simultaneously. Therefore, oxygen vacancies could be introduced into I-D/A ZnO during the annealing process due to the reduction effect of AA on ZnO, and C-doping could be created in I-D/A ZnO via diffusion of carbon species from AA decomposition.

The photoelectrochemical response was investigated in the electrolyte at 0.4 V versus Ag/AgCl (Figure S3A). It showed that the photocurrent of I-D/A ZnO was 1.7 times higher than that of ZnO, while the result of UV−vis diffuse reflectance spectroscopy (UV−vis DRS) indicated that the absorbance and band gaps (∼3.14 eV) of two samples were similar (Figure S3B,C). Thus, variations on light absorption are not the main reasons for improving the photoelectrochemical response of I-D/A ZnO. To investigate the reasonable explanation for enhancement of performances, carrier dynamic behavior in different samples was discussed.

The open-circuit photovoltage decay (OCPVD) was used to analyze the lifetimes of photogenerated carriers (τ) in accordance with the following equation (Figure 4A)[6,44]

$$\tau = \frac{k_B T}{e}\left(\frac{dV_{OC}}{dt}\right)^{-1} \quad (1)$$

where k_B is the Boltzmann constant, T is the thermodynamic temperature, e is the elementary charge, V_{OC} is the open-circuit voltage, and t is the detection time.

According to eq 1, the plots of lifetime versus open-circuit voltage are shown in Figure 4B. It could be found that the lifetime of photogenerated carriers in I-D/A ZnO is longer than that of ZnO. According to Table 1, the lifetime of carries in I-D/A ZnO is about two times longer than that of ZnO, suggesting the synergistic effect of C-doping and oxygen vacancy self-doping on prolonging the carrier lifetime. The electrochemical impedance spectra (EIS) and the equivalent circuit fitting were used to compare the interface electron transfer behaviors of ZnO and I-D/A ZnO (Figure 4C,D). The electron transfer resistance (R2) and the Warburg resistance (W2) were estimated from EIS spectra and are listed in Table 1. Compared with ZnO, R2, and W2 for I-D/A ZnO become

Table 1. Comparison of Electronic Behaviors Between ZnO and I-D/A ZnO

	ZnO	I-D/A ZnO
τ at 0 V (s)	2.36	4.93
R2 (Ohm)	2121	1790
W2 (Ohm·$s^{-1/2}$)	20,800	13,816

https://doi.org/10.1021/acsami.1c07499
ACS Appl. Mater. Interfaces 2021, 13, 33006−33014

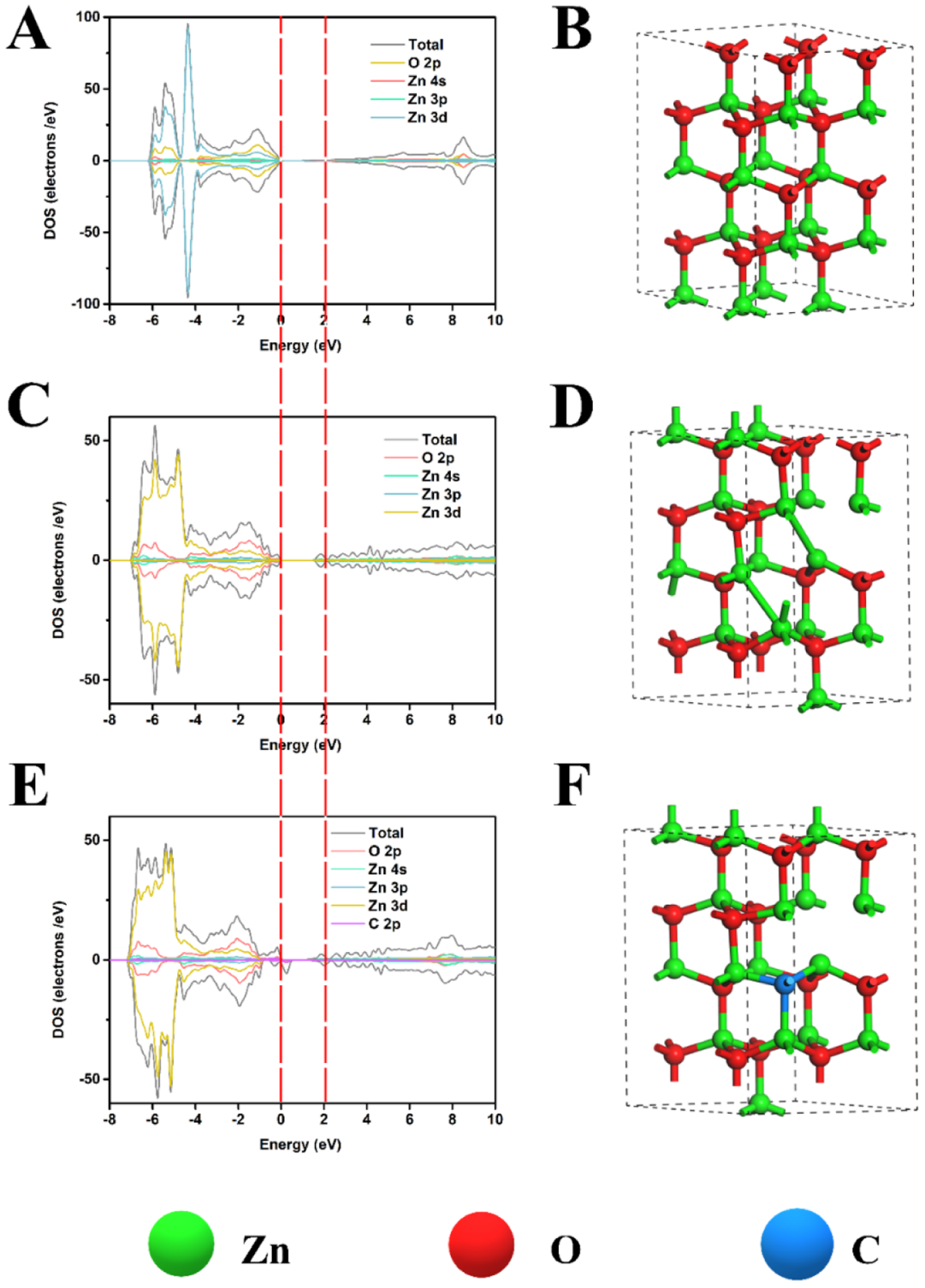

Figure 5. Comparison of the total and projected density of states of (A) ideal ZnO, (C) ZnO, and (E) I-D/A ZnO. The atomic structures of (B) ideal ZnO, (D) ZnO, and (F) I-D/A ZnO.

smaller, suggesting the excellent performance of the interface electron transfer. The reduction of R2 in I-D/A ZnO should be attributed to the co-doping of carbon and oxygen vacancies, while the reduction of W2 should be attributed to the nanoflake structure with nanoparticles.

To comprehensively understand the differences of performances between ZnO and I-D/A ZnO, the resistivity (Table S1) and Mott−Schottky curves (Figure S4) were recorded for analyzing their conductive and carrier concentration. As shown in Table S1, the resistance of ZnO is higher than that of I-D/A ZnO. According to law of resistance, the resistivity could be estimated. Also, the results show that the resistivity of ZnO (0.033 Ω·cm) is lower than that (0.041 Ω·cm) of I-D/A ZnO, which suggests a better electric conduction toward ZnO. On the other hand, Mott−Schottky claimed the higher carrier density (N_D) in ZnO, which is in accordance with the

https://doi.org/10.1021/acsami.1c07499
ACS Appl. Mater. Interfaces 2021, 13, 33006−33014

resistivity results. All these results imply that I-D/A ZnO is a donor−acceptor compensated semiconductor, and further proof and discussion will be shown by DFT calculations.

The electronic densities of state (DOSs) in ideal ZnO (i-ZnO), ZnO, and I-D/A ZnO were calculated with the DFT. According to the calculation results, a band gap of ∼2 eV (Figure 5A) could be obtained for i-ZnO (Figure 5B), which is much smaller than the experimental value (∼3.27 eV). This result is attributed to the shortcoming of the GGA function in DFT calculation.[45,46] When the oxygen vacancy was introduced (Figure 5C), the projected density of states (PDOS) of O 2p in the CB is reduced; however, the PDOS of Zn is expanded to the position below the CBM as a donor level. This result suggests that ZnO is the n-type semiconductor with a smaller band gap (3.14 eV according to the experiment). Compared with ZnO, introduction of carbon into ZnO (Figure 5E) could not only create new acceptor levels, which composed of the PDOS of C 2p and O 2p above the VBM, but also remain the donor level, which composed of the PDOS of Zn below the CBM. In other words, the donor level and acceptor level coexist in I-D/A ZnO. This result proved that I-D/A ZnO is the donor−acceptor compensated semiconductor. The conclusion is consistent well with the photoluminescence spectroscopy, resistivity, and Mott−Schottky test results.

Furthermore, compared with ZnO, I-D/A ZnO shows a higher DOS near the Fermi level (Figure 5C,E), which may provide more electrons for taking part in the electrochemical reactions. Moreover, the asymmetry DOS near the VBM and CBM in I-D/A ZnO implies that unpaired electrons are allowed to exist in I-D/A ZnO (Figure 5E), which would increase the electrochemical reaction activity. As a result, I-D/A ZnO shows the better photoelectrochemical performance.

On the other hand, the acceptor and donor levels play synergistic roles in enhancing the photoelectrochemical performance of I-D/A ZnO. In fact, the acceptor and donor levels could stabilize photogenerated holes and photogenerated electrons, respectively. As a result, the photogenerated excitons could be easily dissociated by the donor−acceptor levels, and the recombination of photogenerated carriers could be effectively hindered, which may prolong the lifetime of carries, statistically.

To evaluate the application potential of I-D/A ZnO in the photoelectrochemical biosensors, the glucose enzyme biosensor was constructed as a model. For the preparation of a photoelectrode, Au NPs were decorated on the electrode to immobilize GOD and enhance the photoelectrochemical performance due to the surface plasmon resonance (SPR), which is similar to the gas sensor.[47,48] The detection was processed with the competition mechanism in the electrolyte containing AA according to our previous work.[49] AA as a core reagent could introduce a competitive response to improve the performance of the glucose photoelectrochemical biosensor, and the detection mechanism is described in detail as follows.

In the case of the electrolyte without glucose, AA will be oxidized into dehydroascorbic acid (DHAA) by photogenerated holes (equation 2 in Figure 6), and photogenerated electrons in the CB will flow throughout the external circuit to form a stable photocurrent response. In this state, the photocurrent response is the strongest. Once glucose was added in the electrolyte, glucose will be oxidized into gluconic acid and H_2O_2 by GOD (equation 3 in Figure 6). The generated H_2O_2 will reduce the photocurrent through the

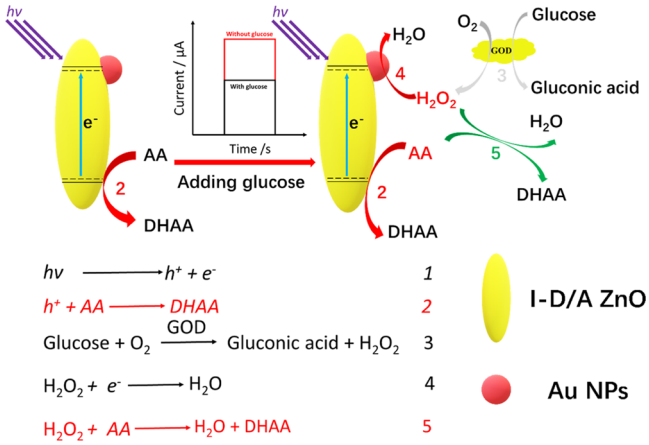

Figure 6. Detection mechanism for the glucose photoelectrochemical biosensor and the related reaction equations.

following two paths: (1) H_2O_2 could be reduced by the photogenerated electrons in the CB (equation 4 in Figure 6) and thus the photocurrent would be abated because of the consumption of photogenerated electrons in the CB; (2) H_2O_2 could react with AA to produce H_2O and DHAA (equation 5 in Figure 6), cutting down the concentration of AA at the electrode surface. As a consequence, the reaction rate of photohole-induced oxidation of AA will be decreased (equation 2 in Figure 6), and thus, the photocurrent would be further reduced. In this detection system, as both H_2O_2 and photogenerated holes could consume AA, a competitive response could be built between equations 2 and 5 in Figure 6, which could be used to effectively detect the concentration of glucose. Also, photocurrent weakened with the increase of glucose concentration.

Figure 7A shows that the photoelectrochemical responses decreased with the increase of the concentration of glucose (Figure 7B), and the responses include two linear ranges (0−10 and 10−15 mM). A high sensitivity of 8.58 $\mu A \cdot cm^{-2} \cdot mM^{-1}$ and a low limit of detection of 39 μM (S/N = 3) could be observed at the low concentration range (0−10 mM), and a sensitivity of 3.86 $\mu A \cdot cm^{-2} \cdot mM^{-1}$ and a limit of detection up to 15 mM could be found at the high concentration range (10−15 mM). In summary, the glucose photoelectrochemical biosensor consisting of I-D/A ZnO shows a good performance with the large detection range up to 15 mM, low limit of detection of 39 μM, and considerable sensitivity of 8.58 $\mu A \cdot cm^{-2} \cdot mM^{-1}$ in low concentration (0−10 mM). Meanwhile, the glucose photoelectrochemical biosensor based on ZnO was analyzed under the same condition (Figure 7C,D). As a result, the lower sensitivity of 6.49 $\mu A \cdot cm^{-2} \cdot mM^{-1}$, higher limit of detection of 360 μM (S/N = 3), and the narrower linear range from 1 to 8 mM could be obtained, which shows poor performance than that of the biosensor based on I-D/A ZnO. These results imply that I-D/A ZnO is a better material than ZnO for the photoelectrochemical biosensor. At last, the detection performances were given in previous literature reports (Table S2) and were used for comparison. It is found that the photoelectrochemical biosensor-based I-D/A ZnO toward glucose shows good performance in sensitivity and detection linear range.

To further evaluate the performance of the glucose enzyme photoelectrochemical biosensor-based I-D/A ZnO, anti-interference capability and stability tests were carried out.

https://doi.org/10.1021/acsami.1c07499
ACS Appl. Mater. Interfaces 2021, 13, 33006−33014

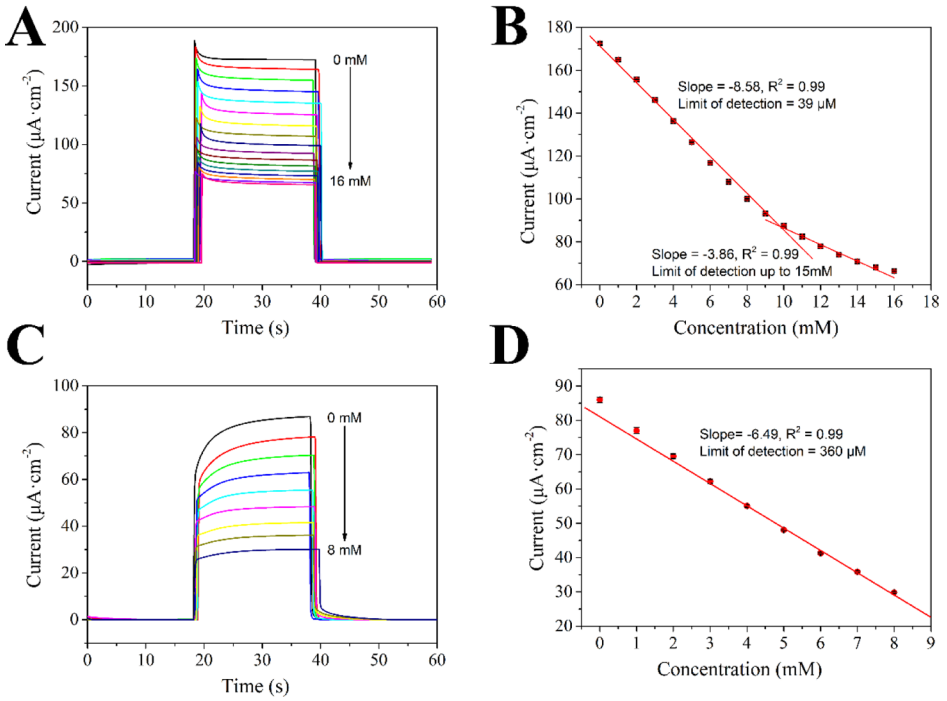

Figure 7. Photoelectrochemical responses with different concentrations of glucose of I-D/A ZnO (A) and ZnO (C) and the calibration curves between the photocurrent and the concentration of glucose of I-D/A ZnO (B) and ZnO (D).

The stability was determined by measuring the photoelectrochemical response 10 times under the same conditions, and the result shows excellent stability with a low RSD of 2.8%. For analyzing the anti-interference capability, NaCl, dopamine, AA, and sucrose were selected as the references. Also, the concentration of NaCl was 1 mM, and those of others were one-tenth that of glucose. The photoelectrochemical response of glucose was set as 100%. As shown in Figure S5, the photoelectrochemical responses of references were −0.47% for NaCl, −4.67% for dopamine, 4.43% for AA, and −3.15% for sucrose. All of them were lower than 5%, which suggest the fine anti-interference capability toward NaCl, dopamine, AA, and sucrose. Meanwhile, the application of the biosensor based on I-D/A ZnO in serum was assessed. The serum was not pretreated, except diluted with the electrolyte. The actual concentration of glucose was detected in the hospital through the hexokinase method. As a result, the recovery of the sample was 104.5% for 4.4 mM. In summary, the biosensor based on I-D/A ZnO shows good performance with high sensitivity, low limit of detection, excellent stability, and fine anti-interference capability, which is mainly attributed to the coexistence of donor levels and acceptor levels, which optimizes carrier behaviors of I-D/A ZnO.

4. CONCLUSIONS

I-D/A ZnO with the coexistence of C-dopants and oxygen vacancies was successfully prepared with the assistance of ascorbic acid. C dopants and oxygen vacancies result in the coexistence of donor and acceptor levels in I-D/A ZnO, which has been proven through the analysis of DOS according to DFT calculations. I-D/A ZnO with an asymmetry DOS exhibits the prolonged carrier lifetime and reduced electron transfer resistance, resulting in an enhanced photoelectrochemical performance. Finally, the excellent photoelectrochemical detection performances toward glucose suggest that I-D/A ZnO is a promising semiconductor for applications on photoelectrochemical biosensors.

■ ASSOCIATED CONTENT

Supporting Information

The Supporting Information is available free of charge at https://pubs.acs.org/doi/10.1021/acsami.1c07499.

SEM and HRTEM images, photoelectric responses, UV-vis DRS, PL spectra, Mott−Schottky plot, and anti-interference of the electrode (PDF)

■ AUTHOR INFORMATION

Corresponding Authors

Chao Zhen − *Shenyang National Laboratory for Materials Science, Institute of Metal Research, Chinese Academy of Sciences, Shenyang 110016, China;* orcid.org/0000-0002-2828-6122; Email: czhen@imr.ac.cn

Jinchun Tu − *Key Laboratory of Advanced Materials of Tropical Island Resources, State Key Laboratory of Marine Resource Utilization in South China Sea, Hainan University, Haikou 570228, China;* orcid.org/0000-0001-8793-4727; Email: tujinchun@hainanu.edu.cn

Authors

Delun Chen − *Key Laboratory of Advanced Materials of Tropical Island Resources, State Key Laboratory of Marine Resource Utilization in South China Sea, Hainan University, Haikou 570228, China*

Xue Zou − *Key Laboratory of Advanced Materials of Tropical Island Resources, State Key Laboratory of Marine Resource Utilization in South China Sea, Hainan University, Haikou 570228, China*

Fan Dong − *Key Laboratory of Advanced Materials of Tropical Island Resources, State Key Laboratory of Marine*

Resource Utilization in South China Sea, Hainan University, Haikou 570228, China

Dan Xiao − *Key Laboratory of Green and Technology, Ministry of Education, College of Chemistry and College of Chemical Engineering, Sichuan University, Chengdu 610065, China;* orcid.org/0000-0001-5295-0540

Xiaohong Wang − *Key Laboratory of Advanced Materials of Tropical Island Resources, State Key Laboratory of Marine Resource Utilization in South China Sea, Hainan University, Haikou 570228, China*

Qiang Wu − *School of Tropical Medicine and Laboratory Medicine, MOE Key Laboratory of Emergency and Trauma, Hainan Medical University, Haikou 571199, China*

Yang Cao − *Key Laboratory of Advanced Materials of Tropical Island Resources, State Key Laboratory of Marine Resource Utilization in South China Sea, Hainan University, Haikou 570228, China; Key Laboratory of Child Cognition & Behavior Development of Hainan Province, Qiongtai Normal University, Haikou 571127, China*

Complete contact information is available at: https://pubs.acs.org/10.1021/acsami.1c07499

Notes

The authors declare no competing financial interest.

■ ACKNOWLEDGMENTS

We thank Chinese Academy of Medical Sciences for the support. This research was financially supported by the National Natural Science Foundation of China (nos. 51762012, 82060386, 51862006, and 52072377), Finance Science and Technology Project of Hainan Province (nos. ZDYF2019161, 2018106, and 2019RC221), and Key laboratory and trauma (Hainan Medical University), Ministry of Education (grant. KLET-201910), and Youth Innovation Promotion Association of the Chinese Academy of Sciences (no. 2020192).

■ REFERENCES

(1) Zhang, M.; Shang, Q.; Wan, Y.; Cheng, Q.; Liao, G.; Pan, Z. Self-Template Synthesis of Double-Shell TiO_2@ZIF-8 Hollow Nanospheres via Sonocrystallization with Enhanced Photocatalytic Activities in Hydrogen Generation. *Appl. Catal., B* **2019**, *241*, 149−158.

(2) Wang, Y.; Tang, J.; Peng, Z.; Wang, Y.; Jia, D.; Kong, B.; Elzatahry, A. A.; Zhao, D.; Zheng, G. Fully Solar-Powered Photoelectrochemical Conversion for Simultaneous Energy Storage and Chemical Sensing. *Nano Lett.* **2014**, *14*, 3668−3673.

(3) Liang, X.; Huang, B.; Wang, Y.; Li, C.; Liu, X.; Huang, M.; Li, H. Photoelectrocatalytic Oxidation of Ascorbate Promoted by Glucose and Tris-(hydroxylmethyl)-amino Methane on Cadmium Sulfide/Titanium Dioxide Electrodes for Efficient Visible Light-enhanced Fuel Cells. *Electrochim. Acta* **2018**, *280*, 332−339.

(4) Tian, C.; Liu, J.; Ruan, R.; Tian, X.; Lai, X.; Xing, L.; Su, Y.; Huang, W.; Cao, Y.; Tu, J. Sandwich Photothermal Membrane with Confined Hierarchical Carbon Cells Enabling High-Efficiency Solar Steam Generation. *Small* **2020**, *16*, 2000573.

(5) Tang, J.; Kong, B.; Wang, Y.; Xu, M.; Wang, Y.; Wu, H.; Zheng, G. Photoelectrochemical Detection of Glutathione by IrO_2−Hemin−TiO_2 Nanowire Arrays. *Nano Lett.* **2013**, *13*, 5350−5354.

(6) Xin, Y.; Li, Z.; Zhang, Z. Photoelectrochemical Aptasensor for the Sensitive and Selective Detection of Kanamycin Based on Au Nanoparticle Functionalized Self-Doped TiO_2 Nanotube Arrays. *Chem. Commun.* **2015**, *51*, 15498−15501.

(7) Song, X.; Hou, T.; Lu, F.; Wang, Y.; Liu, J.; Li, F. Homogeneous Photoelectrochemical Biosensing via Synergy of G-Quadruplex/Hemin Catalysed Reactions and the Inner Filter Effect. *Chem. Commun.* **2020**, *56*, 1811−1814.

(8) Hou, T.; Xu, N.; Wang, W.; Ge, L.; Li, F. Truly Immobilization-Free Diffusivity-Mediated Photoelectrochemical Biosensing Strategy for Facile and Highly Sensitive MicroRNA Assay. *Anal. Chem.* **2018**, *90*, 9591−9597.

(9) Jiang, B.; Li, F.; Yang, C.; Xie, J.; Xiang, Y.; Yuan, R. Target-Induced Catalytic Hairpin Assembly Formation of Functional Y-junction DNA Structures for Label-Free and Sensitive Electrochemical Detection of Human Serum Proteins. *Sens. Actuators, B* **2017**, *244*, 61−66.

(10) Yang, C.; Dou, B.; Yang, J.; Yuan, R.; Xiang, Y. Cross-Triggered and Cascaded Recycling Amplification for Ultrasensitive Electrochemical Sensing of the Mutant Human p53 Gene. *Chem. Commun.* **2016**, *52*, 8707−8710.

(11) Liu, X.; Huo, X.; Liu, P.; Tang, Y.; Xu, J.; Ju, H. TiO_2 Nanowire Arrays Modified with a Simultaneous "Etching, Doping and Deposition" Technique for Ultrasensitive Amperometric Immunosensing. *Biosens. Bioelectron.* **2017**, *92*, 171−178.

(12) Zhu, J.; Huo, X.; Liu, X.; Ju, H. Gold Nanoparticles Deposited Polyaniline−TiO_2 Nanotube for Surface Plasmon Resonance Enhanced Photoelectrochemical Biosensing. *ACS Appl. Mater. Interfaces* **2016**, *8*, 341−349.

(13) Zheng, L.; Han, S.; Liu, H.; Yu, P.; Fang, X. Hierarchical MoS_2 Nanosheet@TiO_2 Nanotube Array Composites with Enhanced Photocatalytic and Photocurrent Performances. *Small* **2016**, *12*, 1527−1536.

(14) Antolini, E. Photo-assisted Methanol Oxidation on Pt-TiO_2 Catalysts for Direct Methanol Fuel cells: A Short Review. *Appl. Catal., B* **2018**, *237*, 491−503.

(15) Liu, J.; Bai, H.; Wang, Y.; Liu, Z.; Zhang, X.; Sun, D. D. Self-Assembling TiO_2 Nanorods on Large Graphene Oxide Sheets at a Two-Phase Interface and Their Anti-Recombination in Photocatalytic Applications. *Adv. Funct. Mater.* **2010**, *20*, 4175−4181.

(16) Liu, J.; Xu, H.; Xu, Y.; Song, Y.; Lian, J.; Zhao, Y.; Wang, L.; Huang, L.; Ji, H.; Li, H. Graphene Quantum Dots Modified Mesoporous Graphite Carbon Nitride with Significant Enhancement of Photocatalytic Activity. *Appl. Catal., B* **2017**, *207*, 429−437.

(17) Zhang, Y.; Zhou, J.; Chen, X.; Feng, Q.; Cai, W. MOF-Derived C-Doped ZnO Composites for Enhanced Photocatalytic Performance Under Visible Light. *J. Alloys Compd.* **2019**, *777*, 109−118.

(18) Pan, L.; Muhammad, T.; Ma, L.; Huang, Z.-F.; Wang, S.; Wang, L.; Zou, J.-J.; Zhang, X. MOF-derived C-Doped ZnO Prepared via a Two-Step Calcination for Efficient Photocatalysis. *Appl. Catal., B* **2016**, *189*, 181−191.

(19) Lv, Y.; Pan, C.; Ma, X.; Zong, R.; Bai, X.; Zhu, Y. Production of Visible Activity and UV Performance Enhancement of ZnO Photocatalyst via Vacuum Deoxidation. *Appl. Catal., B* **2013**, *138*−*139*, 26−32.

(20) Su, C.-Y.; Hsueh, Y.-C.; Kei, C.-C.; Lin, C.-T.; Perng, T.-P. Fabrication of High-activity Hybrid Pt@ZnO Catalyst on Carbon Cloth by Atomic Layer Deposition for Photoassisted Electro-Oxidation of Methanol. *J. Phys. Chem. C* **2013**, *117*, 11610−11618.

(21) Zhang, F.; Wang, X.; Ai, S.; Sun, Z.; Wan, Q.; Zhu, Z.; Xian, Y.; Jin, L.; Yamamoto, K. Immobilization of Uricase on ZnO Nanorods for a Reagentless Uric Acid Biosensor. *Anal. Chim. Acta* **2004**, *519*, 155−160.

(22) Sun, Y.; Fuge, G. M.; Fox, N. A.; Riley, D. J.; Ashfold, M. N. R. Synthesis of Aligned Arrays of Ultrathin ZnO Nanotubes on a Si Wafer Coated with a Thin ZnO Film. *Adv. Mater.* **2005**, *17*, 2477−2481.

(23) Chang, Q.-Q.; Cui, Y.-W.; Zhang, H.-H.; Chang, F.; Zhu, B.-H.; Yu, S.-Y. C-Doped ZnO Decorated with Au Nanoparticles Constructed from the Metal−Organic Framework ZIF-8 for Photodegradation of Organic Dyes. *RSC Adv.* **2019**, *9*, 12689−12695.

(24) Wen, J.-Q.; Tong, X.; Lei, Y.-T.; Tian, P.-H.; Wu, H.; He, W.-L.; Zhang, J.-M. Ferromagnetism Induced by C Doped Graphene-Like ZnO Films with Different Concentrations. *Solid State Commun.* **2019**, *299*, 113663.

(25) Ansari, S. A.; Khan, M. M.; Kalathil, S.; Nisar, A.; Lee, J.; Cho, M. H. Oxygen Vacancy Induced Band Gap Narrowing of ZnO Nanostructures by an Electrochemically Active Biofilm. *Nanoscale* **2013**, *5*, 9238−9246.
(26) Purbayanto, M. A. K.; Nurfani, E.; Chichvarina, O.; Ding, J.; Rusydi, A.; Darma, Y. Oxygen Vacancy Enhancement Promoting Strong Green Emission through Surface Modification in ZnO Thin Film. *Appl. Surf. Sci.* **2018**, *462*, 466−470.
(27) Wang, J.; Chen, R.; Xiang, L.; Komarneni, S. Synthesis, Properties and Applications of ZnO Nanomaterials with Oxygen Vacancies: A Review. *Ceram. Int.* **2018**, *44*, 7357−7377.
(28) Sun, Y.; Zong, Y.; Feng, J.; Li, X.; Yan, F.; Lan, Y.; Zhang, L.; Ren, Z.; Zheng, X. Oxygen Vacancies Driven Size-dependent d^0 Room Temperature Ferromagnetism in Well-Dispersed Dopant-free ZnO Nanoparticles and Density Functional Theory Calculation. *J. Alloys Compd.* **2018**, *739*, 1080−1088.
(29) Kosco, J.; Bidwell, M.; Cha, H.; Martin, T.; Howells, C. T.; Sachs, M.; Anjum, D. H.; Gonzalez Lopez, S.; Zou, L.; Wadsworth, A.; Zhang, W.; Zhang, L.; Tellam, J.; Sougrat, R.; Laquai, F.; DeLongchamp, D. M.; Durrant, J. R.; McCulloch, I. Enhanced Photocatalytic Hydrogen Evolution from Organic Semiconductor Heterojunction Nanoparticles. *Nat. Mater.* **2020**, *19*, 559−565.
(30) Liu, X. T.; Wang, K.; Chang, Z.; Zhang, Y. H.; Xu, J.; Zhao, Y. S.; Bu, X. H. Engineering Donor-Acceptor Heterostructure Metal-Organic Framework Crystals for Photonic Logic Computation. *Angew. Chem. Int. Ed.* **2019**, *58*, 13890−13896.
(31) Lan, Z. A.; Zhang, G.; Chen, X.; Zhang, Y.; Zhang, K. A. I.; Wang, X. Reducing the Exciton Binding Energy of Donor−Acceptor-Based Conjugated Polymers to Promote Charge-Induced Reactions. *Angew. Chem. Int. Ed.* **2019**, *58*, 10236−10240.
(32) Liu, D.; El-Zohry, A. M.; Taddei, M.; Matt, C.; Bussotti, L.; Wang, Z.; Zhao, J.; Mohammed, O. F.; Di Donato, M.; Weber, S. Long-Lived Charge-Transfer State Induced by Spin-Orbit Charge Transfer Intersystem Crossing (SOCT-ISC) in a Compact Spiro Electron Donor/Acceptor Dyad. *Angew. Chem. Int. Ed.* **2020**, *59*, 11591−11599.
(33) Yu, F.; Wang, Z.; Zhang, S.; Ye, H.; Kong, K.; Gong, X.; Hua, J.; Tian, H. Molecular Engineering of Donor-Acceptor Conjugated Polymer/g-C_3N_4 Heterostructures for Significantly Enhanced Hydrogen Evolution under Visible-Light Irradiation. *Adv. Funct. Mater.* **2018**, *28*, 1804512.
(34) Zhou, W.; Jia, T.; Zhang, D.; Zheng, Z.; Hong, W.; Chen, X. The Enhanced Co-catalyst Free Photocatalytic Hydrogen Evolution and Stability Based on Indenofluorene-Containing Donor-Acceptor Conjugated Polymer Dots/g-C_3N_4 Nanosheets Heterojunction. *Appl. Catal., B* **2019**, *259*, 118067.
(35) Song, X.; Li, X.; Zhang, X.; Wu, Y.; Ma, C.; Huo, P.; Yan, Y. Fabricating C and O Co-Doped Carbon Nitride with Intramolecular Donor-Acceptor Systems for Efficient Photoreduction of CO_2 to CO. *Appl. Catal., B* **2020**, *268*, 118736.
(36) Wang, K.; Huang, L.; Eedugurala, N.; Zhang, S.; Sabuj, M. A.; Rai, N.; Gu, X.; Azoulay, J. D.; Ng, T. N. Wide Potential Window Supercapacitors Using Open-Shell Donor−Acceptor Conjugated Polymers with Stable N-Doped States. *Adv. Energy Mater.* **2019**, *9*, 1902806.
(37) Qing, M.; Chen, S. L.; Han, L.; Yang, Y. Z.; Luo, H. Q.; Li, N. B. Three−dimensional Donor−Acceptor−Type Photoactive Material/Conducting Polyaniline Hydrogel Complex for Sensitive Photocathodic Enzymatic Bioanalysis. *Biosens. Bioelectron.* **2020**, *158*, 112179.
(38) Han, Y.; Xing, Z.; Ma, P.; Li, S.; Wang, C.; Jiang, Z.; Chen, Z. Design Rules for Improving the Cycling Stability of High-Performance Donor-Acceptor-Type Electrochromic Polymers. *ACS Appl. Mater. Interfaces* **2020**, *12*, 7529−7538.
(39) Zhi, Y.; Ma, S.; Xia, H.; Zhang, Y.; Shi, Z.; Mu, Y.; Liu, X. Construction of Donor-Acceptor Type Conjugated Microporous Polymers: A Fascinating Strategy for the Development of Efficient Heterogeneous Photocatalysts in Organic Synthesis. *Appl. Catal., B* **2019**, *244*, 36−44.
(40) Toby, B. H. EXPGUI, A Graphical User Interface for GSAS. *J. Appl. Crystallogr.* **2001**, *34*, 210−213.
(41) Zeng, H.; Ning, X.; Li, X. An Insight into Defect Relaxation in Metastable ZnO Reflected by a Unique Luminescence and Raman Evolutions. *Phys. Chem. Chem. Phys.* **2015**, *17*, 19637−19642.
(42) Lu, X.; Wang, G.; Xie, S.; Shi, J.; Li, W.; Tong, Y.; Li, Y. Efficient Photocatalytic Hydrogen Evolution Over Hydrogenated ZnO Nanorod Arrays. *Chem. Commun.* **2012**, *48*, 7717−7719.
(43) Yang, Y.; Han, S.; Zhou, G.; Zhang, L.; Li, X.; Zou, C.; Huang, S. Ascorbic-acid-assisted Growth of High Quality M@ZnO: A Growth Mechanism and Kinetics Study. *Nanoscale* **2013**, *5*, 11808−11819.
(44) Bisquert, J.; Zaban, A.; Greenshtein, M.; Mora-Seró, I. Determination of Rate Constants for Charge Transfer and the Distribution of Semiconductor and Electrolyte Electronic Energy Levels in Dye-Sensitized Solar Cells by Open-Circuit Photovoltage Decay Method. *J. Am. Chem. Soc.* **2004**, *126*, 13550−13559.
(45) Yu, W.; Zhang, J.; Peng, T. New Insight into the Enhanced Photocatalytic Activity of N-, C- and S-Doped ZnO Photocatalysts. *Appl. Catal., B* **2016**, *181*, 220−227.
(46) Perdew, J. P.; Levy, M. Physical Content of the Exact Kohn-Sham Orbital Energies: Band Gaps and Derivative Discontinuities. *Phys. Rev. Lett* **1983**, *51*, 1884−1887.
(47) Mahanti, M.; Basak, D. Enhanced Ultraviolet Photoresponse in Au/ZnO Nanorods. *Chem. Phys. Lett.* **2014**, *612*, 101−105.
(48) Gogurla, N.; Sinha, A. K.; Santra, S.; Manna, S.; Ray, S. K. Multifunctional Au-ZnO Plasmonic Nanostructures for Enhanced UV Photodetector and Room Temperature NO Sensing Devices. *Sci. Rep.* **2014**, *4*, 6483.
(49) Chen, D.; Wang, X.; Zhang, K.; Cao, Y.; Tu, J.; Xiao, D.; Wu, Q. Glucose Photoelectrochemical Enzyme Sensor Based on Competitive Reaction of Ascorbic Acid. *Biosens. Bioelectron.* **2020**, *166*, 112466.

https://doi.org/10.1021/acsami.1c07499
ACS Appl. Mater. Interfaces 2021, 13, 33006−33014